JOURNAL OF GEOPHYSICAL RESEARCH, VOL. 115, D02104, doi:10.1029/2009JD012735, 2010

Maintenance of tropical tropopause layer cirrus

T. P. Dinh,[1] D. R. Durran,[1] and T. P. Ackerman[1]

Received 25 June 2009; revised 30 August 2009; accepted 18 September 2009; published 21 January 2010.

[1] A two-dimensional cloud resolving model with explicit bin microphysics is used to study the maintenance of tropical tropopause layer (TTL) cirrus. Numerical simulations using this model show that a TTL cirrus with a maximum radiative heating rate of 3 K/day is able to self-maintain for as long as 2 days if it contains ice crystals whose initial mean radius is smaller than about 5 μm. The key to the maintenance of the cloud is the circulation thermally forced by the cloud radiative heating. When the cloud layer is at ice saturation and temperature decreases with height, advection of water vapor by the thermally forced circulation results in water vapor flux convergence in the cloud. This leads to growth of ice crystals despite the diabatic warming produced by the radiative heating. The source of water vapor for the growth of ice crystals is outside the cloud lateral edge, which is outside the vertical column that contains the initial cloud. The conversion of water vapor into ice in the simulated TTL cirrus indicates its potential to dehydrate the surrounding environment. This dehydration mechanism does not involve adiabatic cooling associated with external large-scale uplift.

Citation: Dinh, T. P., D. R. Durran, and T. P. Ackerman (2010), Maintenance of tropical tropopause layer cirrus, *J. Geophys. Res.*, *115*, D02104, doi:10.1029/2009JD012735.

1. Introduction

[2] Subvisible cirrus, here defined as cirrus having optical depths less than 0.02, are observed frequently in the upper troposphere. The largest fraction of these thin, high, cold, and icy clouds occurs in the tropics, just below the tropopause [*Wang et al.*, 1996]. Over the equatorial region, subvisible cirrus may occur as frequently as 30% of the time [*Mace et al.*, 2009]. Subvisible cirrus in the tropical tropopause layer (TTL), subsequently referred to as TTL cirrus, are generally only several hundred meters thick, but hundreds of kilometers wide and may persist for as long as a few days [*Winker and Trepte*, 1998].

[3] TTL cirrus have been suggested to be important in the radiative balance of the TTL and in the transport of air and water vapor from the troposphere to the stratosphere. The radiative heating rate in a single-layer TTL cirrus is generally a few Kelvins per day, which is an order of magnitude higher than in cloud-free conditions [*Jensen et al.*, 1996a; *Comstock et al.*, 2002]. Such an increase in the local radiative heating rate could produce vertical motions that result in perturbations of the lower stratospheric circulation [*Gage et al.*, 1991]. Radiatively driven lofting of air in TTL cirrus may be responsible for a significant fraction of troposphere-to-stratosphere mass transport [*Corti et al.*, 2006]. Freeze drying in TTL cirrus of air rising across the tropopause may contribute to the dehydration of the stratosphere [*Jensen et al.*, 1996b].

[4] In this work, we investigate the mechanism responsible for the persistence of TTL cirrus, which is currently not understood. *Ackerman et al.* [1988] suggested, by a scale analysis, that the radiative heating in anvil outflow cirrus in the TTL is primarily used to lift the anvils, rather than to warm the local air. Based on theoretical reasonings, *Lilly* [1988] argued that the radiatively induced mesoscale lifting of an anvil outflow plume helps to preserve cloud ice and predicted the ascent of the plume into the stratosphere. On the other hand, *Boehm et al.* [1999] found, based on their results of two-dimensional (2D) cloud resolving simulations, that the radiatively induced circulation is inadequate to explain TTL cirrus persistence and suggested that TTL cirrus is maintained by externally forced large-scale uplift. However, their conclusion was based on simulations in which the cloud spans the whole horizontal domain. Consequently, the development of cloud-scale circulations with rising motion within the cloud and compensating subsidence outside is inhibited.

[5] Recently, *Durran et al.* [2009] studied the gravity wave circulation thermally forced by the radiative heating of TTL cirrus, both theoretically and by using a 2D dynamical model. Their results suggest that the thermally induced vertical motions can offset sedimentation of ice crystals and also lead to adiabatic cooling that partly counteracts the diabatic warming. However, their model is incomplete because it does not account for microphysical processes including diffusional growth and sedimentation of ice crystals. The diabatic warming in the presence of the cloud circulation, though smaller than that which would otherwise occur if all the radiative heating were used to warm the air, is nonzero. Can TTL cirrus in fact persist in the presence of ice crystal sedimentation and weak diabatic warming? To answer this question it is necessary to build a model in

[1]Department of Atmospheric Sciences, University of Washington, Seattle, Washington, USA.

0148-0227/10/2009JD012735$09.00

which dynamics, microphysics, and radiation processes are allowed to interact continuously.

[6] In this work, the model used by *Durran et al.* [2009] is extended to include an explicit bin microphysics scheme and is then used to explore the interactions of microphysics, dynamics, and radiation in TTL cirrus. The model description and initial conditions of numerical simulations are provided in section 2, followed by the discussion in section 3 of the simulated evolution of a TTL cirrus in an initially motionless atmosphere. The simulated cloud persists for at least two days, indicating that it is self-maintained; there is no requirement for external forcing. The cloud ice mass is not only maintained but is growing with time, despite the diabatic warming. The mechanism responsible for the growth of cloud ice and the origin of the water vapor necessary for such growth are investigated in sections 4 and 5. Section 6 contains predictions for cloud dissipation and sensitivity tests to the size of ice crystals. Section 7 contains the conclusion.

2. Model Description and Initial Conditions

2.1. Model Description

[7] The dynamical and radiative transfer schemes used in this work are the same as in the 2D model used by *Durran et al.* [2009]. The dynamical solver is based on the two–time step compressible formulation presented by *Durran and Klemp* [1983]. The selective-monotonicity-preserving advection scheme [*Blossey and Durran*, 2008] is used to advect potential temperature and moisture variables. Moisture variables relevant to TTL cirrus are ice and water vapor.

[8] The radiative transfer solver [*Durran et al.*, 2009] computes the heating rate due to the absorption of radiation by ice crystals. Scattering effects are negligible and are ignored because TTL cirrus are optically thin. The absorption cross sections of ice crystals are parameterized on the basis of the radiative transfer model introduced by *Toon et al.* [1989] and later updated by *Kato et al.* [1999]. There are two parameterized absorption cross sections for each ice crystal size: the longwave absorption cross section for the 3.3–1000 μm wavelengths, and the shortwave absorption cross section for the 0.24–4.6 μm wavelengths.

[9] In the model the cloud is treated as a perturbation from the background state. Only the motion induced by the absorption of radiation by the cloud ice crystals is computed, while the large-scale, slow motion induced by the radiative transfer of the background atmospheric gases is not. The atmospheric gases are, however, included in the computation of the radiative upward flux at the bottom of the cloud layer and the downward flux at the top of the cloud layer. The two fluxes are used, together with the parameterized absorption of radiation by the cloud ice, to compute the upward flux at the top of the cloud layer and the downward flux at the bottom of the cloud layer.

[10] The current model extends the ice cloud physics by including a bin microphysics solver in which ice crystals are assumed spherical and arranged according to their size into 10 bins. Let r_j^{bin}, $j = 1, \ldots, 11$, denote the radii of ice crystals at the bin boundaries. Ice crystals are neglected if they decay to smaller than r_1^{bin}. We use $r_1^{\mathrm{bin}} = 1$ μm and choose $r_2^{\mathrm{bin}}, \ldots, r_{11}^{\mathrm{bin}}$ for each simulation so as to completely cover the range of crystal sizes that may be present during that simulation.

[11] The microphysics solver performs diffusional growth and sedimentation of ice crystals. The hybrid, postgrowth linear method [*Chen and Lamb*, 1994] is used to perform bin shifts and explicitly calculate evolution of crystal size distribution due to diffusional growth. Ice nucleation is neglected because the supersaturation never exceeds 7% at any time in our simulations. To produce significant homogeneous ice nucleation at temperatures as cold as the tropical tropopause, the supersaturation must be over 60% [*Koop et al.*, 2000].

[12] The assumed spherical shape of ice crystals allows simple calculations of the diffusional growth rate and the sedimentation speed. The diffusional growth rate is calculated based on the formulation

$$\frac{dm}{dt} = \frac{4\pi r(S_{\mathrm{ice}} - 1)}{\dfrac{R_{\mathrm{v}}T}{e_{\mathrm{sat,ice}}D'_{\mathrm{v}}} + \dfrac{L_s}{k'_{\mathrm{a}}T}\left(\dfrac{L_s}{R_{\mathrm{v}}T} - 1\right)} \tag{1}$$

[*Pruppacher and Klett*, 1978], where m and r are, respectively, the mass and radius of ice crystals, S_{ice} is the saturation ratio with respect to ice, R_{v} is the gas constant for water vapor, L_{s} is the latent heat of sublimation, k'_{a} is the modified thermal conductivity of air, D'_{v} is the modified diffusivity of water vapor in air, $e_{\mathrm{sat,ice}}$ is the saturation vapor pressure over plane ice surface, and T is temperature. The sedimentation speed V_{t} is calculated based on

$$V_{\mathrm{t}} = \frac{\eta \mathcal{R}}{2\rho_{\mathrm{a}} r} \tag{2}$$

[*Böhm*, 1989], where η and ρ_{a} are the air viscosity and density, r is the radius of ice crystals, and $\mathcal{R}$ is the Reynold number.

2.2. Model Configuration and Initial Conditions of the Control Simulation

[13] The control simulation is an initial value problem starting with an ice cloud in a motionless atmosphere. There is no imposed large-scale ascent. The cloud is assumed to be symmetric about a vertical axis through its center. With this symmetry it is necessary to do computations for only half of the domain. Here we solve for the right half of the domain and let the cloud center be at $x = 0$, $z = 16.25$ km and the cloud half width and total depth be 80 km and 500 m, respectively. The width of the cloud in the simulation (160 km) is limited by computational cost and is in the smaller range of real TTL cirrus, which are observed to range from 25 km up to 2700 km wide [*Winker and Trepte*, 1998; *Lawson et al.*, 2008].

[14] The computational domain is 0–200 km in the horizontal and 12.5–18.0 km in the vertical. The radiation boundary condition [*Bougeault*, 1983; *Klemp and Durran*, 1983] for hydrostatic gravity waves is imposed at the top boundary. A damping layer between $z = 12.5$ km and 14.5 km prevents waves from reflecting off the lower boundary back into the domain. The western boundary is subject to symmetry boundary condition. The eastern

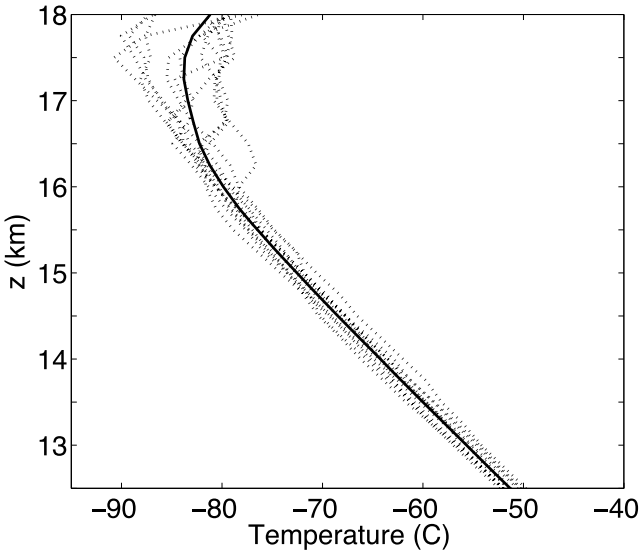

Figure 1. Nauru soundings. The dotted lines are 12 different soundings of January 2007. The solid line is the average of the actual soundings and is used as the temperature profile in the model simulations.

boundary is subject to outflow boundary condition at a gravity wave phase speed of 5.5 m s^{-1}.

[15] The grid spacings are Δx = 100 m and Δz = 25 m everywhere in the domain except in the damping layer. Δz is stretched from 25 m at z = 14.5 km (top of the damping layer) to 100 m at z = 12.5 km (bottom of the domain and of the damping layer). The large dynamical time step is 6 s and the small dynamical time step is 0.3 s. Since microphysical processes are not tightly linked to the dynamics, it is possible to save computational time by computing the microphysics in a longer time step than the dynamical time step. Thus, advection of ice and water vapor, diffusional growth, and sedimentation of ice crystals are performed every 16 large time steps. Test cases where microphysical processes are computed every 6 s or 16 × 6 s = 96 s show almost no difference.

[16] The atmospheric profile used in the simulation is an average of 12 different January 2007 balloon-borne soundings at Nauru island. The sounding data are obtained from the Atmospheric Radiation Measurement (ARM) Program website (http://www.arm.gov/). Nauru island (0.521°S, 166.916°E) is located in the tropical western Pacific, close to the region of maximum TTL cirrus coverage reported by *Mace et al.* [2009]. The temperature profiles of the 12 actual soundings and their average are shown in Figure 1. The initial temperature of the average sounding decreases with height everywhere in the computational domain, except in the top layer between 17 and 18 km. With this sounding the initial atmosphere is stable everywhere in the domain. The Brunt-Väisälä frequency in the initial cloud layer (16.0–16.5 km) is 0.016 s^{-1}.

[17] The initial radius of ice crystals is assumed to be r_0 = 3.0 μm in the control simulation. This radius is at the peak of the crystal size distribution in subvisible cirrus observed over the Marshall Islands [see *McFarquhar et al.*, 2000, Figure 1]. The bin configuration is $r_j^{\rm bin} = r_1^{\rm bin} + (j-1)\Delta r^{\rm bin}$, j = 1, . . ., 11, where $\Delta r^{\rm bin}$ = 1.2 μm. The values of $r_j^{\rm bin}$, the corresponding absorption cross sections, and crystal fall speeds are given in Table 1. In the control simulation only a small number of crystals grow to the largest bin, so r_{11} = 13 μm is sufficiently large. For crystals at an intermediate radius between the bin boundaries, the absorption cross sections are computed by interpolation of the parameterized absorption cross sections given in Table 1. Note that the fall speed of spherical crystals is larger than that of crystals having any other shapes at the same volume, so the values in Table 1 represent upper limits of sedimentation.

[18] The cloud is initialized by adding ice crystals into the domain at the initial time. The initial ice mass density is set as $M(x, z, t = 0) = M_0 f(x) g(z)$, where $M_0 = N_0 \rho_{\rm ice} \frac{4}{3}\pi r_0^3$, $N_0 = 1.3 \times 10^6$ m^{-3}, r_0 = 3 μm. The variations of the initial ice mass density in the horizontal and vertical directions are

$$f(x) = \begin{cases} 1 & \text{if } x < a \\ \cos^2\left(\frac{\pi}{2a}(x-a)\right) & \text{if } a \le x \le 2a \\ 0 & \text{otherwise,} \end{cases} \quad (3)$$

where a = 40 km and

$$g(z) = \begin{cases} \cos\left(\frac{\pi}{2d}(z-z_c)\right) & \text{if } z_c - d \le z \le z_c + d \\ 0 & \text{otherwise,} \end{cases} \quad (4)$$

where z_c = 16.25 km and d = 250 m. The initial ice mixing ratio $q_{\rm ice}$ and the initial radiative heating are shown in Figure 2. The radiative heating is, to a good approximation, proportional to $q_{\rm ice}$ because the cloud is optically thin. The contours shown in Figure 2 for $q_{\rm ice}$ and the radiative heating are identical at the current resolution, so only one graph is provided for both quantities. In the middle cloud region between the origin and x = 40 km, the initial radiative heating rate is 3 K/day and the ice absorption optical depth is 0.0067.

[19] The initial saturation ratio $S_{\rm ice}$ is set to be 1.0 in the initial cloud layer between z = 16.0 km and 16.5 km and 0.8 above and below this layer. Thus, in the cloud layer the water vapor mixing ratio is the saturation water vapor

Table 1. Bin Boundary Radii Used for the Control Simulation, the Parameterized Longwave and Shortwave Absorption Cross Sections, and the Sedimentation Speeds Calculated Using Equation (2) at the Temperature and Pressure at the Cloud Center[a]

Radius (μm)	$\sigma_{\rm longwave}$ (μm^2)	$\sigma_{\rm shortwave}$ (μm^2)	Fall Speed (mm s^{-1})
1.0	0.65	0.01	0.19
2.2	6.6	0.10	0.90
3.4	22.	0.30	2.1
4.6	47.	0.61	3.9
5.8	82.	1.0	6.2
7.0	130.	1.5	9.0
8.2	180.	2.2	12.
9.4	250.	3.0	16.
10.6	330.	4.1	20.
11.8	410.	5.4	25.
13.0	510.	6.4	30.

[a]Longwave wavelengths are 3.3–1000 μm, and shortwave wavelengths are 0.24–4.6 μm. At the cloud center, T = −81 C, and p = 108 mb.

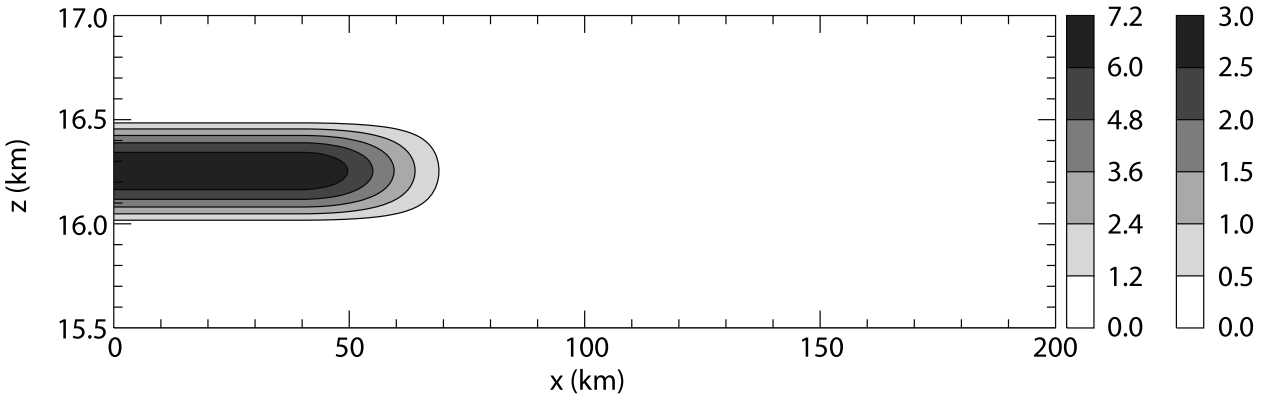

Figure 2. Initial ice mixing ratio (10^{-7} kg/kg) and radiative heating (K/day). The first scale bar (closest to the graph) is for the ice mixing ratio, and the second scale bar is for the radiative heating.

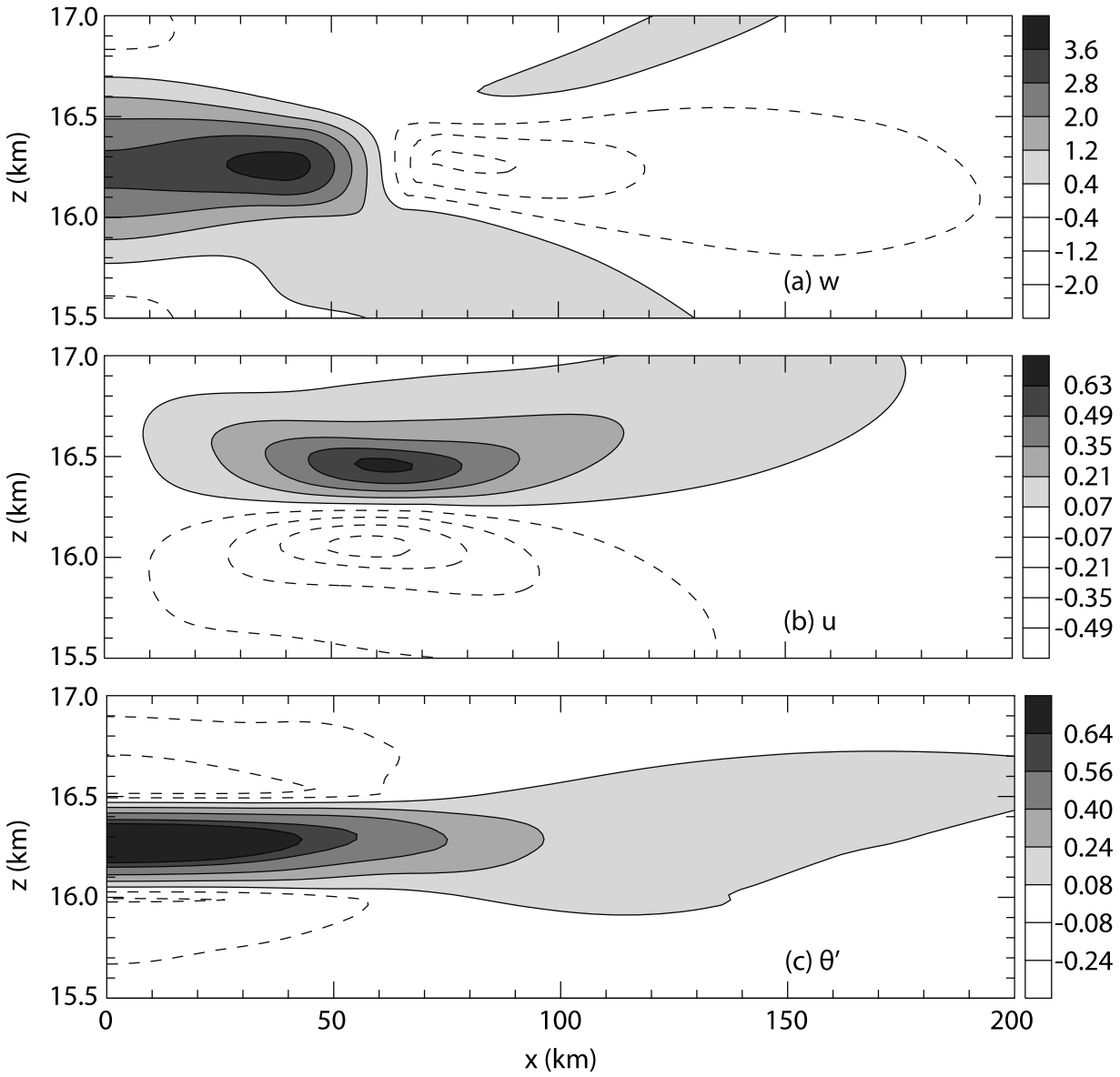

Figure 3. The cloud dynamics at 6 h forced by the radiative heating: (a) vertical velocity (mm s^{-1}), (b) horizontal velocity (m s^{-1}), and (c) potential temperature perturbation (K). Positive values are contoured by solid lines, and negative values are contoured by dashed lines.

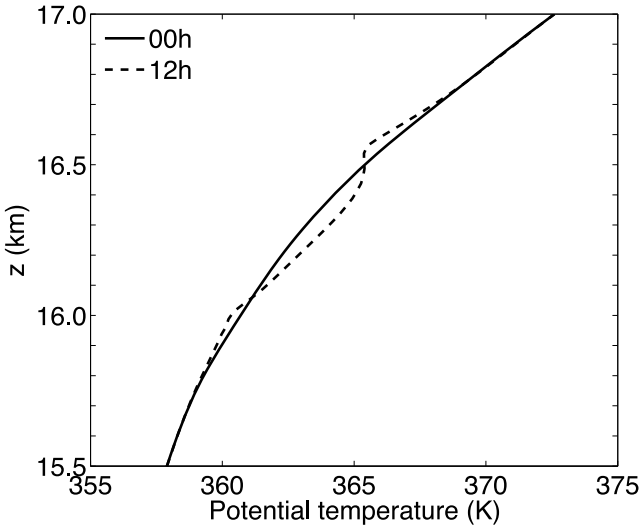

Figure 4. Potential temperature at the cloud center ($x = 0$) at $t = 0$ and $t = 12$ h.

mixing ratio, which decreases with height because temperature decreases with height.

3. Dynamics and Evolution of the Cloud in the Control Simulation

3.1. Circulation Induced by the Radiative Heating

[20] The heat that results from the absorption of radiation by ice crystals is expected to produce both rising vertical motions and warming of the local air. Horizontal motions arising in connection with these vertical motions are also expected by the conservation of mass. The cloud circulation and the local temperature change induced by TTL cirrus radiative heating were discussed in detail by *Durran et al.* [2009]. They are shown here at hour 6 of our simulation (Figure 3).

[21] The thermally forced circulation consists of rising vertical motions mostly within the cloud and compensating sinking motions outside the cloud lateral edge. Horizontal motions include inflow toward the cloud base and outflow from its top, which tend to narrow the cloud base and widen the top. Rising vertical motions are mostly concentrated in the cloud where direct heating is present, whereas horizontal motions extend far outside (compare Figure 2 with Figures 3a and 3b).

[22] Temperature perturbations are produced not only inside but also outside the cloud lateral edge (Figure 3c). Warming inside the cloud is a direct result of the diabatic heating, whereas warming outside the cloud between $x =$ 70 km and 200 km is produced by the adiabatic warming of subsiding air. There is weak adiabatic cooling above and below the heated layer as rising motions extend slightly above the cloud top and below the cloud base. The change in the potential temperature along a vertical profile through the cloud center ($x = 0$) is shown in Figure 4. At 12 h a shallow unstable layer between $z = 16.45$ km and 16.55 km has been created as a result of the diabatic warming within the cloud and the adiabatic cooling in the rising air just above the cloud top.

[23] Convection begins around 12.5 h in the destabilized layer at the cloud top as weak perturbations in the vertical velocity field (Figure 5a), then quickly develops into alternating rising and sinking cells whose vertical motion amplitudes are stronger than the background cloud circulation (Figures 5b and 5c). Newborn convective cells (Figure 5b) are roughly 800 m (8 grid cells) across and extend throughout the unstable layer between $z = 16.45$ km and 16.55 km. The cells are initially regular (Figure 5b) and later become irregular (Figure 5c).

[24] Buoyancy forces associated with these convective cells generate gravity waves which propagate upward above the convective layer and downward below it. Phase lines of positive and negative vertical velocities in the convectively driven gravity waves tilt eastward with height above the convective layer and westward below it (Figure 5c). Time lapse images (not shown) indicate that convective cells propagate eastward because of the background outflow in the upper half of the cloud layer. The orientation of the convectively driven gravity waves relative to the propagating convective cells is consistent with that discussed by *Fovell et al.* [1992].

3.2. Cloud Evolution

[25] The cloud evolution is shown in Figure 6. The cloud top stretches while its base narrows as ice crystals are transported by the circulation induced by the radiative heating. After about 12.5 h the ice distribution becomes irregular due to the convection at the cloud top. Convection modifies the small-scale structure of the cloud while the thermally forced circulation modulates its overall shape.

[26] The vertical profiles of the horizontally integrated cloud ice mass at $t = 0$, 12 h and 48 h are shown in Figure 7. The cloud center (the level at which the ice mass is maximum) is lifted from $z = 16.25$ km at the initial time to 16.35 km at 12 h, and to above 16.4 km at 48 h. The cloud slowly self-lofts during the simulation because on average rising motions induced by the radiative heating exceed the sedimentation speeds of ice crystals.

[27] Figure 8 shows the evolution of the total ice mass, the total number of ice crystals, the mean crystal radius and the ice mixing ratio q_{ice} averaged over cloudy grid cells. The first two quantities are defined as the domain integrals $M^* = \int\int M\, dx\, dz$ and $N^* = \int\int N\, dx\, dz$, where M (kg m^{-3}) and N (m^{-3}) are the ice mass and number density. The mean crystal radius $\bar{r}$ is defined by $M^*/N^* = \rho_{\text{ice}}\frac{4}{3}\pi\bar{r}^3$. In the first 4 h, which is the model spin up time during which the thermally forced circulation develops from rest, M^*, N^*, and $\bar{r}$ decrease with time. After the spin up time, M^* increases while N^* decreases, so $\bar{r}$ increases with time. The spatially averaged q_{ice} decreases with time, despite the growth of M^*, because the cloud is spreading horizontally. The growth rate of M^* is reduced and the reduction rate of N^* is increased after about 15 h as the convective cells become sufficiently strong to induce significant mixing of dry air from above into the cloud and overshooting of ice crystals at the cloud top.

[28] Figure 9 shows the evolution of the ice crystal size distribution. The number of crystals on the vertical axis is the domain integral $\int\int N_j\, dx\, dz$, where N_j is the number density in the j^{th} bin. Since ice crystals grow or sublimate at different rates in different regions of the cloud, the size distribution

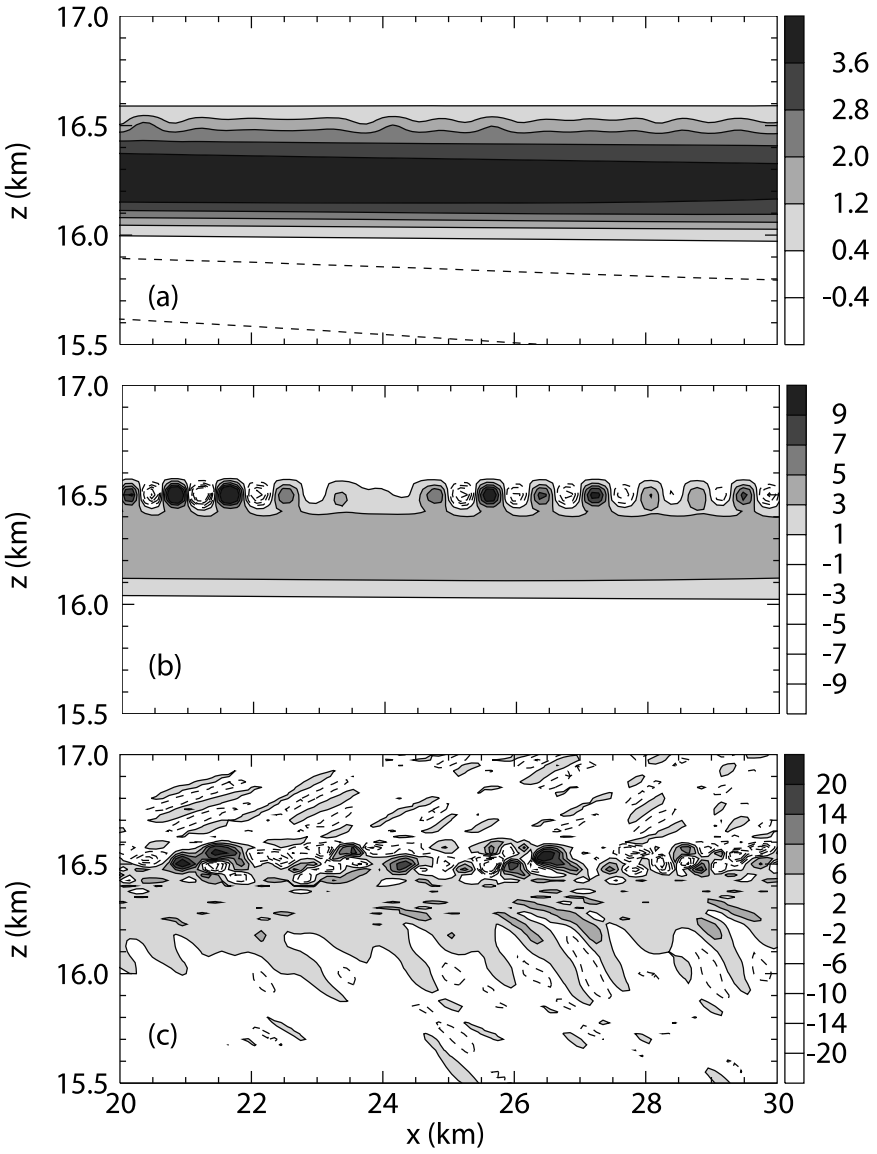

Figure 5. Vertical velocity (mm s^{-1}) at (a) $t \approx 12.5$ h, (b) $t \approx 13.5$ h, and (c) $t = 20$ h. Positive values are contoured by solid lines, and negative values are contoured by dashed lines.

evolves from monodisperse initially to polydisperse at later times. The maximum crystal size increases with time and the whole distribution shifts gradually toward larger sizes. This is consistent with the growth of $\bar{r}$ (Figure 8c) and indicates that on average ice crystals are growing by deposition. This continued growth is not consistent with the stabilization mechanism proposed by *Luo et al.* [2003], in which ice crystals oscillate about an equilibrium size at which sedimentation is exactly balanced by large-scale upwelling.

4. Mechanism That Maintains the Cloud

4.1. Hypothesis

[29] It is intriguing that ice crystals in the control simulation are not only maintained but are growing by deposition despite the cloud diabatic warming. In contrast to this result, it has generally been assumed that cooling, either diabatic cooling in TTL cirrus over convective anvils [*Hartmann et al.*, 2001] or adiabatic cooling associated with large scale ascent [*Jensen et al.*, 1996b; *Boehm et al.*, 1999], is a necessary condition for ice crystals to grow. To explain the growth of ice crystals in our simulation, we hypothesize that the effects of both sedimentation and diabatic warming are counteracted by the thermally forced cloud circulation.

[30] Within the cloud the thermally forced updraft offsets and at times exceeds the sedimentation speed of ice crystals. For example, at 6 h the mean crystal radius is 2.9 μm (Figure 8c), which corresponds to a fall speed of 1.6 mm s^{-1} according to equation (2). At this time, the updraft is greater than 1.6 mm s^{-1} throughout most of the cloud (Figure 3a). Consequently, the cloud center is lifted from z = 16.25 km at the initial time to 16.35 km at 12 h (Figure 7).

[31] In addition, the updraft induces in-cloud adiabatic cooling and water vapor flux convergence, both of which increase the saturation ratio in the cloud. To illustrate this point, we computed the horizontally integrated rates of change of S_{ice} at 6 h implied by changes in temperature

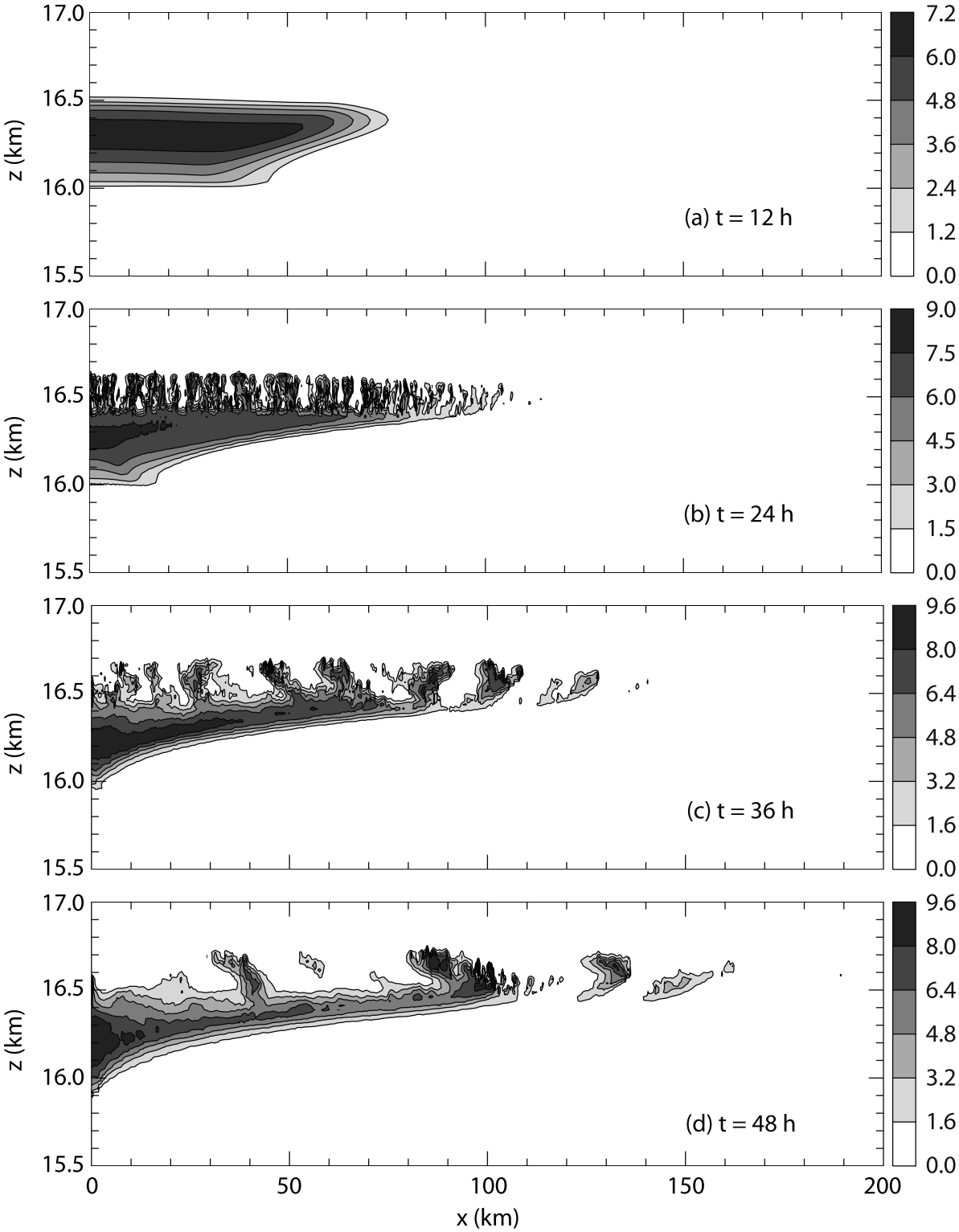

Figure 6. Ice mixing ratio (10^{-7} kg/kg) at 12, 24, 36, and 48 h.

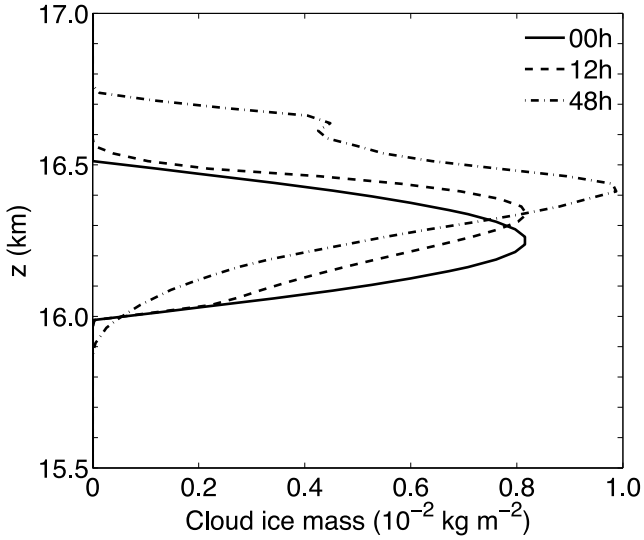

Figure 7. Vertical profiles of the horizontally integrated cloud ice mass at t = 0, 12 h, and 48 h.

($\frac{\partial T}{\partial t}$), and by vertical advection of water vapor ($-w\frac{\partial q_v}{\partial z}$). At this time $|-u\frac{\partial q_v}{\partial x}| \ll |-w\frac{\partial q_v}{\partial z}|$, so $-w\frac{\partial q_v}{\partial z}$ accounts for almost all the water vapor flux convergence. Also, since changes in S_{ice} outside the cloud do not lead to ice sublimation or growth, the rates of change of S_{ice} are integrated over cloudy grid cells only.

[32] The rate of change of S_{ice} implied by $\frac{\partial T}{\partial t}$ is negative in the cloud midlevels and positive in the cloud top and base levels (Figure 10a). Because latent heat release is two orders of magnitude smaller than the radiative heating, $\frac{\partial T}{\partial t}$ is produced primarily by either radiative warming or adiabatic processes. Radiative warming dominates in the cloud midlevels, because the ice density is greatest there, while adiabatic cooling associated with rising motions dominates at the cloud top and base. The rate of change of S_{ice} implied by $\frac{\partial T}{\partial t}$ summed over the whole cloud layer is negative, which indicates that on average adiabatic cooling is not sufficient to counteract diabatic warming.

[33] On the other hand, as also shown in Figure 10a, $\frac{\partial S_{ice}}{\partial t}$ implied by $-w\frac{\partial q_v}{\partial z}$ is positive in most of the cloud layer, except for a thin layer at the cloud base. The sharp positive and negative peaks in $\frac{\partial S_{ice}}{\partial t}$ implied by $-w\frac{\partial q_v}{\partial z}$ at the cloud top

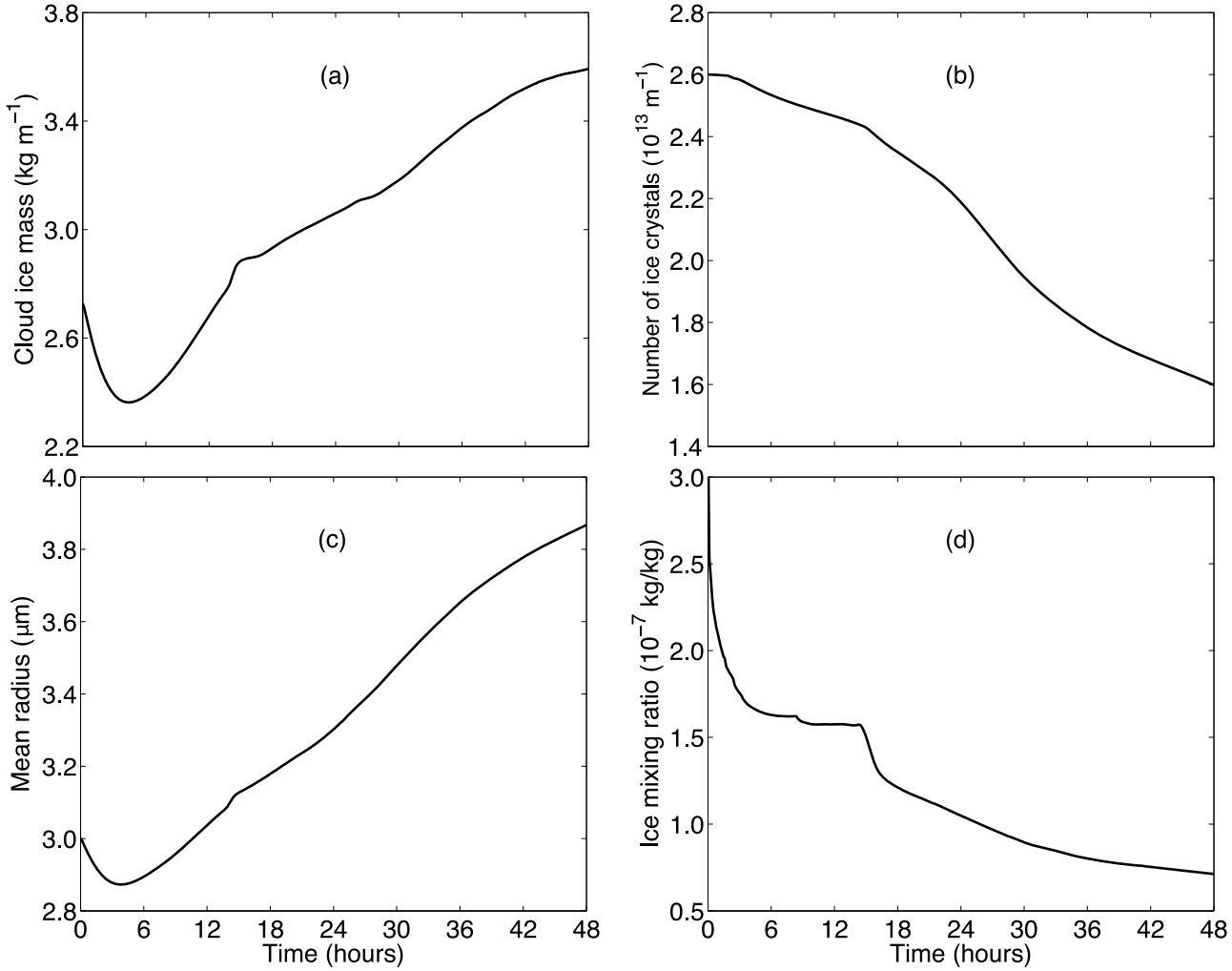

Figure 8. Time dependence of (a) the domain-integrated cloud ice mass M*, (b) the domain-integrated number of ice crystals N*, (c) the mean crystal radius, and (d) the ice mixing ratio averaged over cloudy grid cells.

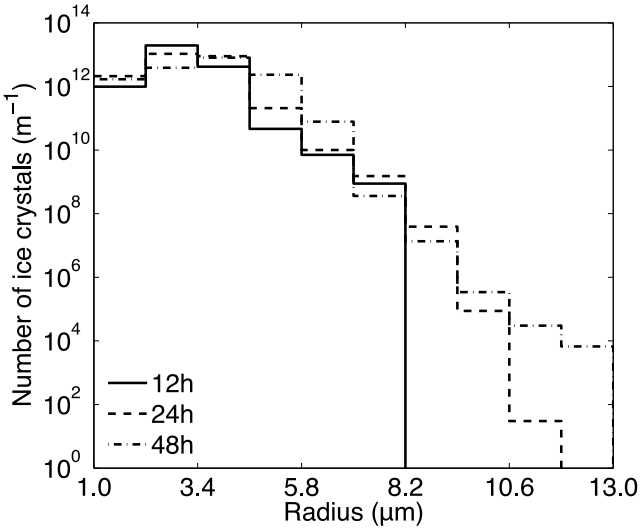

Figure 9. Ice crystal size distribution at 12, 24, and 48 h.

and base are due to the jumps in the q_v profile. These jumps are somewhat artificial because the q_v profile is imposed as an initial condition. There is a local maximum in $\frac{\partial S_{ice}}{\partial t}$ implied by $-w\frac{\partial q_v}{\partial z}$ at z = 16.35 km, slightly above the maximum in the vertical velocity field at this time.

[34] The sum of the two curves in Figure 10a is shown in Figure 10b. The net $\frac{\partial S_{ice}}{\partial t}$ is positive throughout most of the cloud layer. This indicates that the increase in S_{ice} due to water vapor flux convergence exceeds the decrease in S_{ice} due to diabatic warming. Since $S_{ice} \approx 1$ at this time, a tendency for S_{ice} to increase means that ice crystals are growing by deposition. The growth of ice crystals, in turn, keeps S_{ice} close to unity throughout the cloud lifetime.

[35] If ice crystals did not grow by deposition, the cloud region would be moistened due to the convergence of water vapor flux. Moistening of the cloudy atmospheric column by advection of water vapor was also discussed by *Sherwood* [1999]. In his model of cloud "vapor pumping," the cloud-radiative-dynamic processes are hypothetically solved in sequential adjustment steps, rather than simultaneously as in our model. *Sherwood* [1999] assumed that the radiative heating is completely counteracted by adiabatic processes, so the temperature profile is always relaxed to the initial profile after the adjustment processes. This assumption is not correct because, as we have shown in section 3.1, radiative heating produces both diabatic warming and vertical motions. Because of the differences in model constructions and assumptions, the rate of moistening of the cloudy region by advection of water vapor suggested by *Sherwood* [1999] is much larger than what we found using our model.

4.2. Experiment A: Role of Water Vapor Flux Convergence

4.2.1. Initial Conditions

[36] Experiment A is designed to further test the hypothesis that the convergence of water vapor flux in the cloud results in the growth of ice crystals. Two simulations, the no-advection case and the isothermal case, are compared with the control case. In the no-advection case, advection of water vapor, but not of cloud ice, is turned off in the model. In the isothermal case, the initial temperature profile is modified to be constant with height for $z \geq 16$ km (Figure 11a). Since neither the initial S_{ice} nor the temperature changes with height in the cloud layer for the isothermal case, the initial water vapor mixing ratio q_v increases with height within the cloud due to the decrease in pressure with height. The vertical profiles of the initial q_v in the control case and the isothermal case are given in Figure 11b.

[37] The potential temperature profiles of the control case and the isothermal case are shown in Figure 11c. The stability and, therefore, the Brunt-Väisälä frequency in the initial cloud layer are lower in the control case than in the isothermal case. The Brunt-Väisälä frequency in the initial cloud layer is 0.016 s^{-1} and 0.022 s^{-1}, respectively, for the control case and the isothermal case. The thermally forced circulation is inversely proportional to the square of

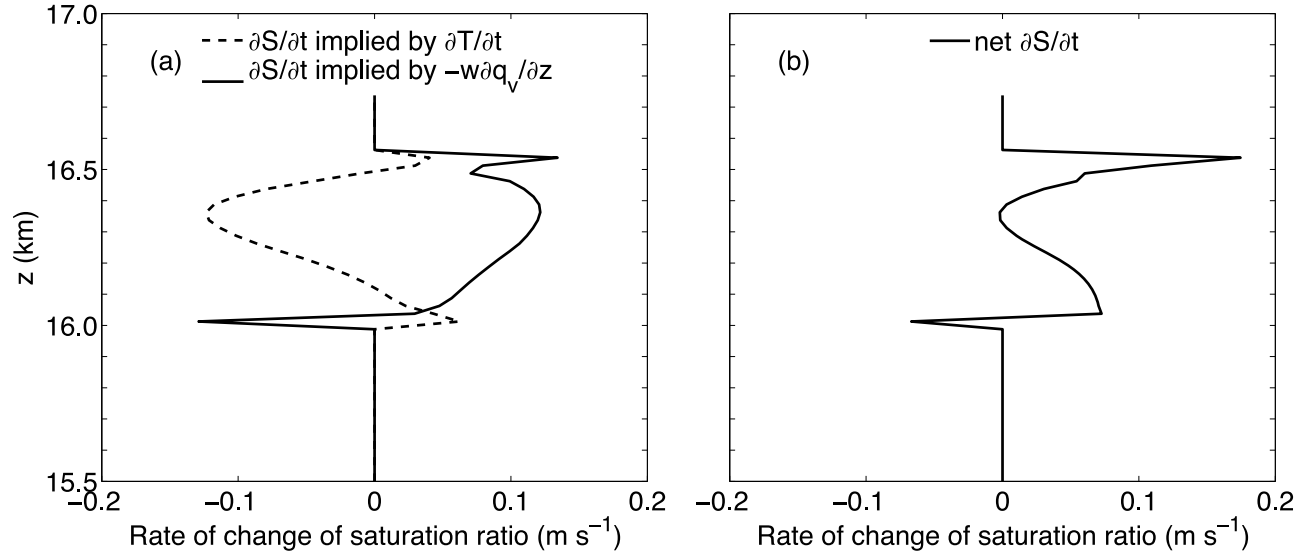

Figure 10. The horizontally integrated rate of change of the saturation ratio in the cloud at 6 h implied by (a) temperature change and vertical advection of water vapor and (b) both effects.

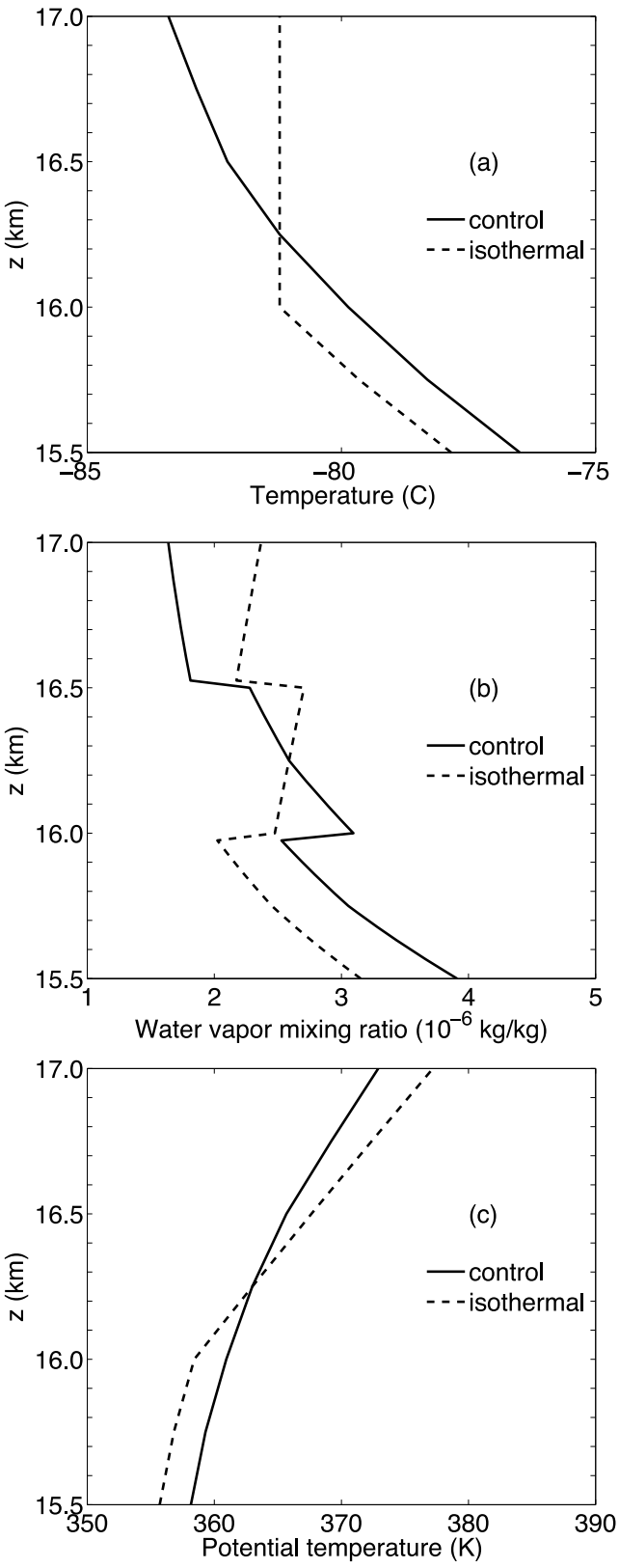

Figure 11. Profiles of (a) initial temperature, (b) initial water vapor mixing ratio, and (c) initial potential temperature of the control case and the isothermal case.

the Brunt-Väisälä frequency and is proportional to the radiative heating [*Durran et al.*, 2009]. Therefore, to produce a circulation of similar magnitude to the control case, we increase the initial radiative heating by increasing the initial cloud ice in the isothermal case. The initial ice number density at the cloud center is 1.3×10^6 m^{-3} for the control case and 2.5×10^6 m^{-3} for the isothermal case. The differences in the initial conditions between the control case and the test cases are summarized in Table 2.

4.2.2. Results and Discussions

[38] The ratios of the total ice mass M^* at the current time to the initial time for the three cases of Experiment A are shown in Figure 12. After a 4 h period of model spin up, M^* increases with time in the control case, but it decreases monotonically in the two test cases.

[39] In the control case, the vertical advection of water vapor produces water vapor flux convergence in the cloud because q_v decreases with height. In this case the effect of water vapor flux convergence (which tends to increase S_{ice}) exceeds the effect of diabatic warming (which tends to decrease S_{ice}), so ice crystals grow. In the no-advection case, water vapor flux convergence is zero, so ice crystals sublimate due to diabatic warming. In the isothermal case, q_v increases with height in the cloud layer, so the vertical advection of water vapor results in water vapor flux divergence in the cloud. This leads to further sublimation of ice crystals in addition to the sublimation induced by diabatic warming. Thus ice crystals disappear faster in the isothermal case than in the no-advection case.

[40] This experiment suggests a necessary condition for TTL cirrus to self-maintain for a long time is that the temperature in the cloud layer decreases with height. Therefore, it is unlikely that TTL cirrus will persist in the stratosphere, where temperature increases with height.

5. Source of Water Vapor for the Growth of Cloud Ice

5.1. Hypothesis

[41] In the preceding section, water vapor flux convergence due to the vertical advection of water vapor was shown to be responsible for the maintenance and growth of ice crystals. One might expect that ice crystals grow by using in-cloud or below-cloud water vapor, brought upward by vertical motions. However, this intuition is not entirely correct because the thermally forced updraft does not extend more than 300 m below the cloud base (Figure 3a). As a consequence, the amount of moisture supplied to the cloud from below is rather limited. We hypothesize that the growth of cloud ice is initially fueled by the water vapor inside the cloud, but that subsequent, continuous growth requires additional moisture which is supplied to the cloud mainly by the horizontal motions.

[42] Figure 13 shows trajectory analyses and cloud boundaries at 24 h, 36 h, and 48 h of the control simulation. All trajectories in the three panels start at $t = 0$, cross the cloud boundaries at the respective times indicated in the panels, and end at 48 h. The trajectories indicate that air is first advected horizontally toward the cloud, then vertically upward once it is inside the cloud. Almost all the air that ends up in the cloud at 48 h originates from within the broad horizontal layer containing the cloud; very little air comes

Table 2. Initial Conditions of the Cases in the Numerical Experiments[a]

Case	Water Vapor Advection	Temperature Profile	S_{ice} i	S_{ice} ii	S_{ice} iii	S_{ice} iv	Initial Radius (μm)
Control	Yes	Figure 1	1.0	1.0	0.8	0.8	3.0
No advection	No	Figure 1	1.0	1.0	0.8	0.8	3.0
Isothermal	Yes	Figure 11	1.0	1.0	0.8	0.8	3.0
Dry edge	Yes	Figure 1	1.0	0.8	0.8	0.8	3.0
Dry bottom	Yes	Figure 1	1.0	1.0	0.8	0.0	3.0
5.0 μm	Yes	Figure 1	1.0	1.0	0.8	0.8	5.0
8.8 μm	Yes	Figure 1	1.0	1.0	0.8	0.8	8.8

[a]Here i is the initial cloud region $x \in [0;80]$ km and $z \in [16.0;16.5]$ km, ii is the region outside and at the same altitude as the initial cloud, and iii and iv are the layer above and below both regions i and ii, respectively.

from below the cloud. The cloud processes water vapor in two steps. First, horizontal motions advect water vapor toward the cloud center. Then, once water vapor is inside the cloud, vertical motions advect water vapor upward, resulting in water vapor flux convergence and ice growth.

[43] The origin of the water vapor taken up by the cloud has important implications for the dehydration effect of TTL cirrus. *Jensen et al.* [1996b] studied TTL cirrus using 1D models in which dehydration is limited to a vertical column of air that undergoes adiabatic cooling in response to some specified large-scale uplift. In contrast, our 2D simulation shows that the cloud dehydrates its surrounding environment without an imposed large-scale uplift, and it primarily dehydrates the air outside its lateral edge, rather than the air below its base. In other words, the dehydration occurs in the horizontal layer containing the cloud, rather than the vertical column containing the cloud. If the cloud persists for a long time, the region containing the water vapor processed by the cloud may be horizontally very nonlocalized.

5.2. Experiment B: Origin of Water Vapor

5.2.1. Initial Conditions

[44] Experiment B is designed to provide further evidence that the origin of the water vapor taken up by the cloud is mainly from outside the initial cloud lateral edge, not from below the initial cloud. The control simulation is compared with two other simulations: the dry bottom case and the dry edge case. In the dry bottom case, S_{ice} below the initial cloud base is reduced, relative to the control case, from 0.8 to 0. Thus there is initially no water vapor below the cloud in the dry bottom case. In the dry edge case, we reduce S_{ice} in the region initially outside the cloud lateral edge from the 1.0 value used in the control case to 0.8. The differences in the initial conditions between the control case and the test cases are summarized in Table 2.

5.2.2. Results and Discussions

[45] The comparison of the total ice mass M^* of the cases in Experiment B is given in Figure 14. M^* is smaller in the dry bottom case than in the control case, but it increases with time after 4 h of model spin up in both cases. This result indicates that the water vapor below the cloud is beneficial but not essential to the maintenance and growth of the cloud.

[46] In the dry edge case M^* increases with time similarly to the control case up to about 24 h, but then it starts to decrease. The difference in these two cases suggests that, in the first 24 h ice growth is fueled by the water vapor that is inside the initial cloud, but after 24 h, this water vapor has decreased to the point that the cloud requires an additional source of water vapor if growth is to continue.

[47] Figure 15 illustrates that the saturation ratio outside the cloud lateral boundary is higher in the control case than in the dry edge case. As horizontal motions continuously advect air toward the cloud base, additional water vapor is supplied to the cloud in the control case because the air outside is sufficiently moist. In the dry edge case, on the other hand, dry air laterally crossing the cloud boundary into the lower half of the cloud contributes to the net sublimation of ice crystals after 24 h.

6. Cloud Dissipation and Sensitivity to Crystal Size

6.1. Dissipation of the Cloud

[48] The lateral edge of the cloud in the control simulation starts to approach the eastern domain boundary at 48 h. Thus, in order to simulate the cloud after 48 h we would need to rerun the simulation in a larger domain. This is not computationally feasible with the current version of the model. Nevertheless, it is possible to predict the general fate

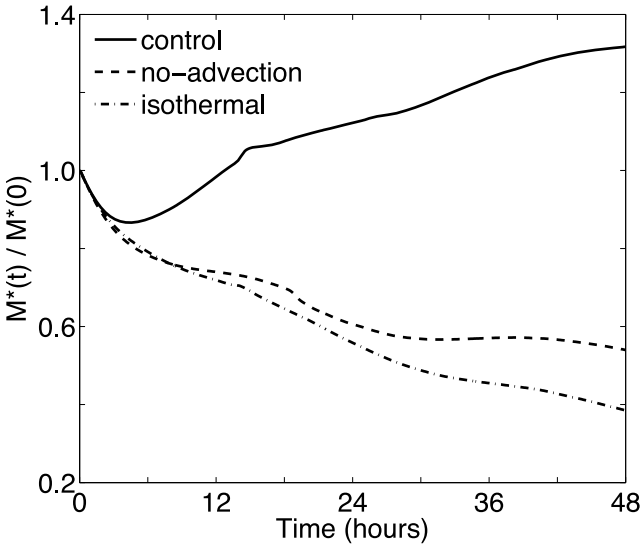

Figure 12. The ratio at the current time to the initial time of the domain-integrated ice mass M^* for the cases in Experiment A.

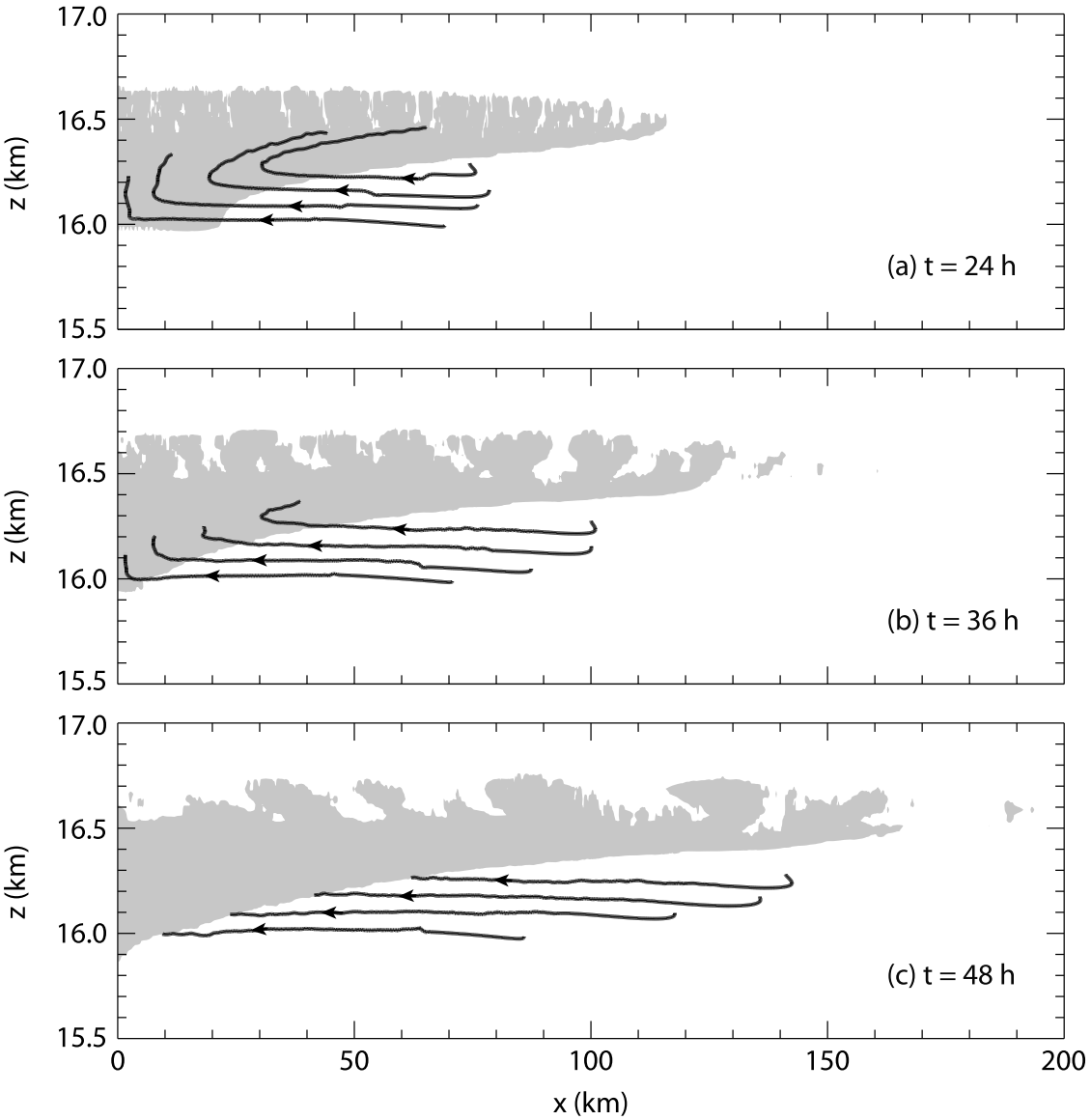

Figure 13. The 48 h trajectories (solid black lines) overlaying the cloud (shaded) at 24 h, 36 h, and 48 h. The trajectories start at $t = 0$ outside the shaded regions, cross the cloud boundaries at the time indicated in each plot, and end at 48 h. Arrowheads indicate the directions of the trajectories.

of the cloud with the information available from the first 48 h.

[49] During the 48 h simulation ice crystals grow by deposition (Figure 8c) and thus their sedimentation speeds increase with time. On the other hand, the spatially averaged ice mixing ratio decreases with time (Figure 8d), which, together with the increase in crystal size, imply that the averaged radiative heating and the thermally forced vertical velocity decrease with time. When the sedimentation speeds of ice crystals exceed the speed of the updraft, ice crystals will fall into the subsaturated layer below the cloud layer and sublimate. If this mechanism is responsible for the dissipation of the cloud, the cloud layer will be dehydrated as water vapor is removed irreversibly from it.

[50] In the idealized control simulation, the cloud lasts for at least 48 h. In reality, insufficient water vapor outside the cloud lateral edge, shear disturbances, or large-scale wave disturbances (that produce warm anomalies in the cloud region) may lead to earlier dissipation of the cloud. Another important factor limiting the cloud lifetime is the initial size of ice crystals. We expect that if the initial ice crystals are larger, their sedimentation speeds are correspondingly larger and the cloud dissipates sooner. The sensitivity of model results to the size of ice crystals is shown next in Experiment C.

6.2. Experiment C: Sensitivity to Crystal Size

6.2.1. Initial Conditions

[51] Experiment C consists of three simulations in which the initial radii of ice crystals are 3.0 μm, 5.0 μm, and 8.8 μm. On the basis of Table 1 and Figure 3a, 5 μm crystals are about the largest crystals whose fall speeds can be counteracted by vertical velocities similar in magnitude to the control case. The 8.8 μm radius is chosen to match the effective radius recently reported by *Lawson et al.* [2008] for observed ice crystals in TTL cirrus over Costa Rica.

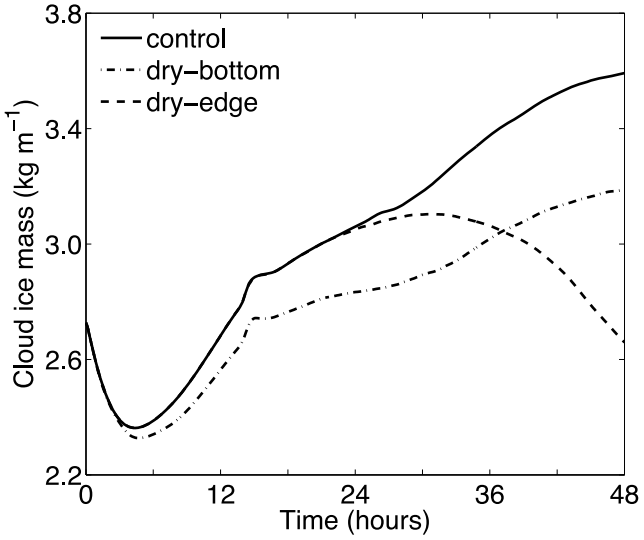

Figure 14. Time dependence of the domain-integrated ice mass for the cases in Experiment B.

[52] In order to cover a wide range of crystal sizes, the radii at the bin boundaries are set to be $r_j^{\mathrm{bin}} = c^{j-1} r_1^{\mathrm{bin}}$, $j = 1, \ldots, 11$, where $c = 50^{\frac{1}{10}}$. This bin configuration covers crystal radii from $r_1^{\mathrm{bin}} = 1$ μm to $r_{11}^{\mathrm{bin}} = 50$ μm. There is no significant difference in the results of the 3.0 μm case whether the wider bin configuration or the bin configuration of the control simulation is used.

[53] Because of the difference in the initial crystal sizes, the initial number density of ice crystals is adjusted so that the initial radiative heating in the test cases is the same as the control case. The initial number density of ice crystals at the cloud center is 3.8×10^5 m^{-3} for the 5.0 μm case and 1.0×10^5 m^{-3} for the 8.8 μm case. The differences in the initial conditions between the control case and the test cases are summarized in Table 2.

6.2.2. Results and Discussions

[54] Figure 16 shows the time dependence over the first 24 h of the total ice mass M^* of the three cases in Experiment C. After the model spin up, M^* increases with time in both the 3.0 μm case and the 5.0 μm case, although the growth rate of M^* is very small in the later case. In contrast, M^* decreases quickly in the 8.8 μm case, in which most of the cloud has dissipated by 24 h.

[55] Vertical profiles of the ice mass at 12 h for the three cases are shown in Figure 17. In the 3.0 μm and 5.0 μm cases, at 12 h the majority of ice remains in the moist layer between $z = 16.0$ and 16.5 km. In the 8.8 μm case, on the other hand, by 12 h most of the ice has fallen below $z = 16.0$ km. In this case ice crystals sublimate as they fall into the subsaturated layer below $z = 16.0$ km.

[56] This experiment indicates that TTL cirrus lifetime depends strongly on the size of ice crystals. We expect that while TTL cirrus containing small crystals can self-maintain for a long time, those containing only large crystals cannot persist without the assistance of large-scale ascent. In TTL cirrus that contain a combination of crystals at different

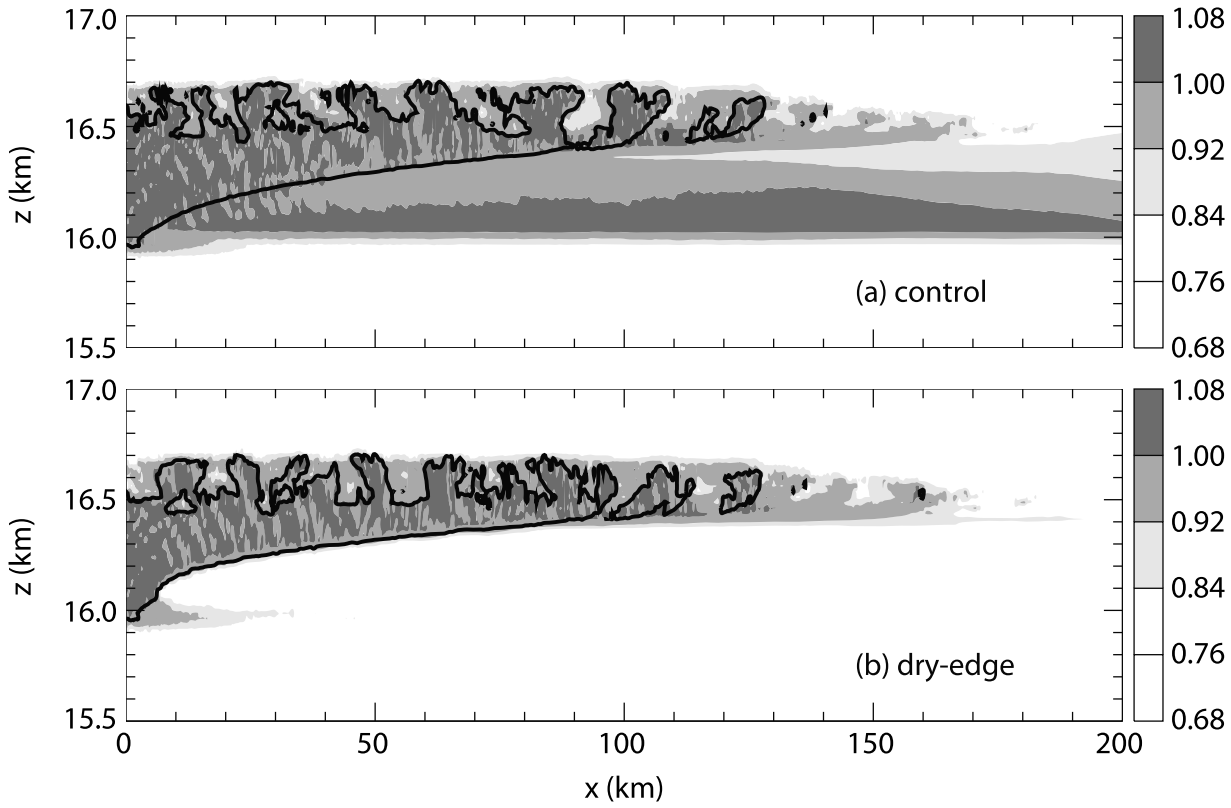

Figure 15. The saturation ratio at 36 h for (a) the control case and (b) the dry edge case. The saturation ratio is shaded in grey scale and is overlayed by the cloud boundary in solid line. The cloud boundary is defined by the 1.6×10^{-7} kg/kg ice mixing ratio contour.

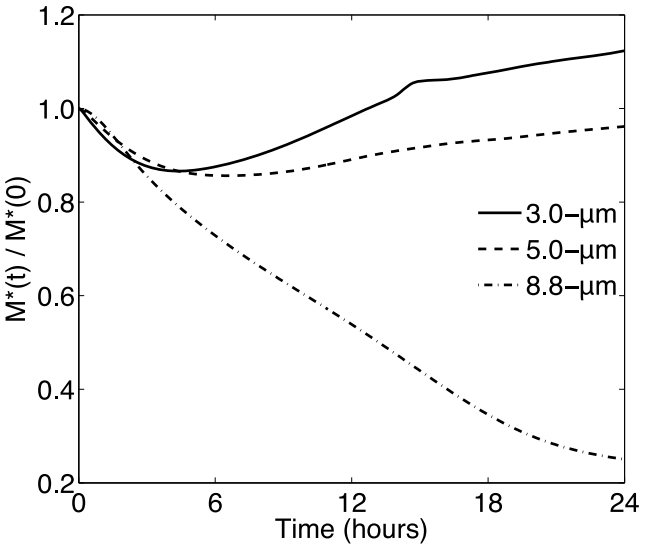

Figure 16. The ratio at the current time to the initial time of the domain-integrated ice mass M^* for the cases in Experiment C.

sizes, larger crystals will fall out first leaving behind smaller ones. In the absence of external forcing, small ice crystals may grow by the mechanism presented in section 4 until they become sufficiently large to sediment out.

7. Conclusion

[57] Our results show that, in the absence of large-scale ascent, tropical tropopause layer (TTL) cirrus can be maintained through the internal interactions of cloud dynamics, radiation, and microphysics. The key to TTL cirrus persistence is the circulation forced by the cloud radiative heating. The thermally forced circulation consists of rising motion within the cloud, accompanied by sinking motion outside, and horizontal inflow toward the cloud base, accompanied by outflow from its top. The circulation acts against ice sublimation by producing water vapor flux convergence in the cloud and against sedimentation by lifting the ice crystals.

[58] Ice crystals do not sublimate if advection of water vapor by the thermally forced circulation produces sufficient in-cloud water vapor flux convergence. If the cloud is approximately at ice saturation, the thermally forced circulation produces water vapor flux convergence as long as the temperature decreases with height. In the control simulation, the effect of water vapor flux convergence to increase the saturation ratio exceeds the effect of diabatic warming to decrease it, so ice crystals must grow in order to keep the saturation ratio at approximate unity. On the other hand, in the stratosphere, where the temperature increases with height, the thermally forced circulation will produce water vapor flux divergence, and TTL cirrus are unlikely to persist.

[59] The cloud in the control simulation is able not only to self-maintain but also to take up water vapor inside and, in particular, outside its lateral edge to grow ice crystals by deposition. Vertical advection of water vapor by the cloud circulation leads to the conversion of water vapor into ice while horizontal advection of water vapor continuously brings additional moisture into the cloud. Since the horizontal velocity field extends well beyond the cloud lateral edge, its tendency to dehydrate the air is horizontally nonlocalized, especially if the cloud persists for a long time. If the surrounding atmosphere is moist (e.g., close to ice saturation), ice crystals grow by deposition until they become sufficiently large to fall below the initial cloud layer, thus irreversibly removing water vapor from this layer.

[60] In the 48 h of the control simulation, the thermally forced updraft is sufficient to counteract ice sedimentation in most of the cloudy region, which leads to slow lifting of the cloud during this period. However, while the ice sedimentation rate increases with time due to the growth in size of ice crystals, the updraft decreases because the spatially averaged radiative heating decreases as the cloud spreads horizontally. Therefore, one factor limiting the cloud lifetime is that ice crystals ultimately grow to a size at which their sedimentation speed exceeds the updraft. Sensitivity tests on the size of ice crystals show that, at a radiative forcing maximum of 3 K/day, the thermally forced updraft is not sufficient to counteract sedimentation of crystals larger than about 5 μm in radius. We expect that while TTL cirrus containing small crystals can self-maintain for a long time, those containing only large crystals cannot persist without the assistance of large-scale ascent. If the clouds initially consist of crystals at different sizes, larger crystals will fall out first leaving behind smaller ones, which may grow by the mechanism that we proposed until they become sufficiently large to sediment out.

[61] An interesting feature shown in detail for the control simulation is the convection at the cloud top. Radiative heating and the thermally induced vertical motion destabilize the shallow layer at the cloud top in which convection occurs, while stabilizing the rest of the cloud layer. Because convection is restricted to the cloud top, the cloud-scale circulation is not destroyed by convection and it continues to maintain and grow ice crystals throughout the rest of the

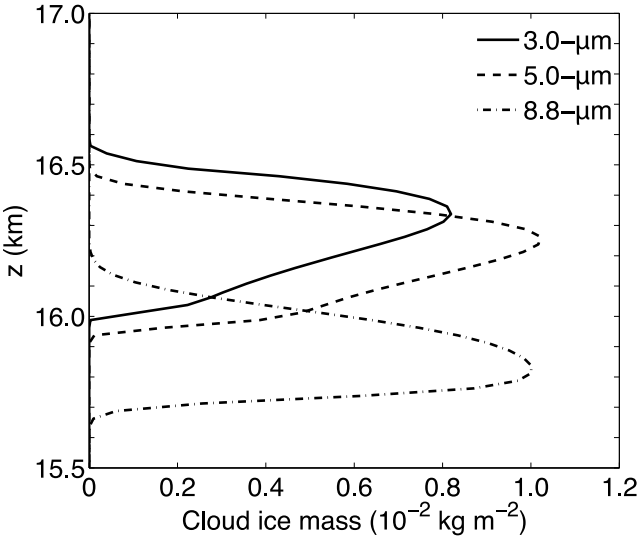

Figure 17. Vertical profiles of the horizontally integrated ice mass at 12 h for the cases in Experiment C.

cloud layer. Convection enhances mixing between in-cloud air and the air just above the cloud top, which results in a reduction of the growth rate of the total ice mass. Convection also causes the ice distribution to become spatially irregular.

[62] The model used in this study is being developed for future research relating to TTL cirrus. One direction for future research is to include ice nucleation into the model so that study of TTL cirrus formation is possible. TTL cirrus microphysical properties such as ice crystal number density and crystal size distribution are determined by the different mechanisms through which the clouds are formed. Explorations of crystal size distributions more realistic than the initially monodisperse distribution used in this work will be carried out in conjunction with study of TTL cirrus formation. In the future, we hope to be able to simulate the complete life cycle, from formation through development and dissipation, of TTL cirrus.

[63] Another research direction that we intend to pursue is to determine the role of TTL cirrus in stratospheric dehydration. This study shows that these clouds can take up water vapor from the surrounding environment to grow ice crystals by deposition, thus potentially playing a role in stratospheric dehydration. Previous research has generally assumed that the conversion of water vapor into ice in TTL cirrus is associated with adiabatic cooling due to vertical ascent, and that the dehydration effect can be modeled in a vertical column of air. On the contrary, we show that dehydration takes place in the horizontal layer containing the cloud, which emphasizes the necessity to study TTL cirrus in multidimensional models. We will attempt to evaluate quantitatively the dehydration of TTL air by thin cirrus using a 3D model. The thermally forced vertical velocity is not expected to be significantly different between 2D and 3D, because it depends primarily on the magnitude of the heating. However, since horizontal motions are distributed in a horizontal plane in 3D (rather than in one direction as in 2D), the horizontal extent of the dehydrated region would be different in a 3D model.

[64] **Acknowledgments.** The authors are grateful to Jennifer Comstock of the Pacific Northwest National Laboratory for many illuminating discussions about the simulation of ice microphysics and two anonymous reviewers for helpful comments. This research was supported by NSF grants ATM-0225441 and ATM-0506589 and the University of Washington Office of Research.

References

Ackerman, T. P., K. N. Liou, F. P. J. Valero, and L. Pfister (1988), Heating rates in tropical anvils, *J. Atmos. Sci.*, *45*(10), 1606–1623.

Blossey, P. N., and D. R. Durran (2008), Selective monotonicity preservation in scalar advection, *J. Comput. Phys.*, *227*, 5160–5183.

Boehm, M. T., J. Verlinde, and T. P. Ackerman (1999), On the maintenance of high tropical cirrus, *J. Geophys. Res.*, *104*(D20), 24,423–24,434.

Böhm, H. P. (1989), A general equation for the terminal fall speed of solid hydrometeors, *J. Atmos. Sci.*, *46*(15), 2419–2427.

Bougeault, P. (1983), A non-reflective upper boundary condition for limited-height hydrostatic models, *Mon. Weather Rev.*, *111*(3), 420–429.

Chen, J.-P., and D. Lamb (1994), Simulation of cloud microphysical and chemical processes using a multicomponent framework: Part I. Description of the microphysical model, *J. Atmos. Sci.*, *51*(18), 2613–2630.

Comstock, J. M., T. P. Ackerman, and G. G. Mace (2002), Ground-based lidar and radar remote sensing of tropical cirrus clouds at Nauru island: Cloud statistics and radiative impacts, *J. Geophys. Res.*, *107*(D23), 4714, doi:10.1029/2002JD002203.

Corti, T., B. P. Luo, Q. Fu, H. Vömel, and T. Peter (2006), The impact of cirrus clouds on tropical troposphere-to-stratosphere transport, *Atmos. Chem. Phys.*, *6*(9), 2539–2547.

Durran, D. R., and J. B. Klemp (1983), A compressible model for the simulation of moist mountain waves, *Mon. Weather Rev.*, *111*(12), 2341–2361.

Durran, D. R., T. Dinh, M. Ammerman, and T. Ackerman (2009), The mesoscale dynamics of thin tropical tropopause cirrus, *J. Atmos. Sci.*, *66*(9), 2859–2873.

Fovell, R., D. Durran, and J. R. Holton (1992), Numerical simulations of convectively generated stratospheric gravity waves, *J. Atmos. Sci.*, *49*(16), 1427–1442.

Gage, K. S., J. R. McAfee, D. Carter, W. L. Ecklund, A. C. Riddle, G. C. Reid, and B. B. Balsley (1991), Long-term mean vertical motion over the tropical pacific: Wind-profiling doppler radar measurements, *Science*, *254*(5039), 1771–1773.

Hartmann, D. L., J. R. Holton, and Q. Fu (2001), The heat balance of the tropical tropopause, cirrus, and stratospheric dehydration, *Geophys. Res. Lett.*, *28*(10), 1969–1972.

Jensen, E. J., O. B. Toon, H. B. Selkirk, J. D. Spinhirne, and M. R. Schoeberl (1996a), On the formation and persistence of subvisible cirrus clouds near the tropical tropopause, *J. Geophys. Res.*, *101*(D16), 21,361–21,375.

Jensen, E. J., O. B. Toon, L. Pfister, and H. B. Selkirk (1996b), Dehydration of the upper troposphere and lower stratosphere by subvisible cirrus clouds near the tropical tropopause, *Geophys. Res. Lett.*, *23*(8), 825–828.

Kato, S., T. P. Ackerman, J. H. Mather, and E. E. Clothiaux (1999), The k-distribution method and correlated-k approximation for a shortwave radiative transfer model, *J. Quant. Spectrosc. Radiat. Transfer*, *62*, 109–121.

Klemp, J. B., and D. R. Durran (1983), An upper boundary condition permitting internal gravity wave radiation in numerical mesoscale models, *Mon. Weather Rev.*, *111*(3), 430–444.

Koop, T., B. Luo, A. Tsias, and T. Peter (2000), Water activity as the determinant for homogeneous ice nucleation in aqueous solutions, *Nature*, *406*, 611–614.

Lawson, R. P., B. Pilson, B. Baker, Q. Mo, E. Jensen, L. Pfister, and P. Bui (2008), Aircraft measurements of microphysical properties of subvisible cirrus in the tropical tropopause layer, *Atmos. Chem. Phys.*, *8*, 1609–1620.

Lilly, D. (1988), Cirrus outflow dynamics, *J. Atmos. Sci.*, *45*(10), 1594–1605.

Luo, B. P., et al. (2003), Ultrathin tropical tropopause clouds (UTTCs): Part II. Stabilization mechanisms, *Atmos. Chem. Phys.*, *3*, 1093–1100.

Mace, G. G., Q. Zhang, M. Vaughan, R. Marchand, G. Stephens, C. Trepte, and D. Winker (2009), A description of hydrometeor layer occurrence statistics derived from the first year of merged Cloudsat and CALIPSO data, *J. Geophys. Res.*, *114*, D00A26, doi:10.1029/2007JD009755.

McFarquhar, G. M., A. J. Heymsfield, J. Spinhirne, and B. Hart (2000), Thin and subvisual tropopause tropical cirrus: Observations and radiative impacts, *J. Atmos. Sci.*, *57*(12), 1841–1853.

Pruppacher, H. R., and J. D. Klett (1978), *Microphysics of Clouds and Precipitation*, 714 pp., D. Reidel, Dordrecht, Netherlands.

Sherwood, S. C. (1999), On moistening of the tropical troposphere by cirrus clouds, *J. Geophys. Res.*, *104*(D10), 11,949–11,960.

Toon, O. B., C. P. McKay, and T. P. Ackerman (1989), Rapid calculation of radiative heating rates and photodissociation rates in inhomogeneous multiple scattering atmospheres, *J. Geophys. Res.*, *94*(D13), 16,287–16,301.

Wang, P.-H., P. Minnis, M. P. McCormick, G. S. Kent, and K. M. Skeens (1996), A 6-year climatology of cloud occurrence frequency from Stratospheric Aerosol and Gas Experiment II observations (1985–1990), *J. Geophys. Res.*, *101*(29), 407–429.

Winker, D. M., and C. R. Trepte (1998), Laminar cirrus observed near the tropical tropopause by LITE, *Geophys. Res. Lett.*, *25*(17), 3351–3354.

T. P. Ackerman, T. P. Dinh, and D. R. Durran, Department of Atmospheric Sciences, University of Washington, 408 ATG Building, Seattle, WA 98195, USA. (ackerman@atmos.washington.edu; tra@atmos.washington.edu; durrand@atmos.washington.edu)